Magnetic behavior of Fe-doped zirconia studied by synchrotron radiation measurements and first-principles simulations

By

Ciprian, R (Ciprian, R.) [1] ; Lamperti, A (Lamperti, A.) [2] ; Capasso, L (Capasso, L.) [1] ; Motti, F (Motti, F.) [3] , [4] ; Cianci, E (Cianci, E.) [2] ; Weschke, E (Weschke, E.) [5] ; Torelli, P (Torelli, P.) [3] ; (.) [2]

PHYSICAL REVIEW MATERIALS

Volume: 4; Issue: 5 Published: MAY 27 2020

Published version is available with

DOI: https://doi.org/10.1103/PhysRevMaterials.4.054417

Addresses

1 Elettra Sincrotrone Trieste, Ss 14,Km 163-5, I-34149 Trieste, Italy

2 CNR, IMM, Agrate Unit, Via C Olivetti 2, I-20864 Agrate Brianza, MB, Italy

3 CNR, Lab TASC, Ist Off Mat IOM, Area Sci Pk,SS 14 Km 163-5, I-34149 Trieste, Italy

4 Univ Milan, Dipartimento Fis, Via Celoria 16, I-20133 Milan, Italy

5 Helmholtz Zentrum Berlin Mat & Energie, Albert Einstein Str 15, D-12489 Berlin, Germany

Magnetic behavior of Fe-doped zirconia studied by synchrotron radiation measurements and first principles simulations

R. Ciprian (1), A. Lamperti (2), L. Capasso (1), F. Motti (3,4),
E. Cianci (2), E. Weschke (5), P. Torelli (3), A. Debernardi (2)

(1) Elettra Sincrotrone di Trieste, s.s. 14,
km 163.5, 34149 Basovizza, Trieste, Italy;

(2) CNR-IMM, Agrate Unit, via C. Olivetti 2, 20864 Agrate Brianza (MB), Italy

(3) Istituto Officina dei Materiali (IOM)-CNR,
Laboratorio TASC, Area Science Park,
S.S. 14 km 163.5, Trieste I-34149, Italy

(4) Dipartimento di Fisica, Universitá degli Studi di Milano,
via Celoria 16, I-20133 Milano, Italy

(5) Helmholtz-Zentrum Berlin für Materialien und Energie,
Albert-Einstein-Str. 15, 12489 Berlin, Germany

(Dated: March 19, 2020)

Abstract

Exploiting first principles simulations and x-ray absorption near edge spectroscopy (XANES) in high magnetic fields, we investigated the magnetic properties of thin films of zirconia doped with Fe impurities. In our $Zr_{1-x}Fe_xO_{2-y}$ samples, grown by atomic layer deposition (ALD), the Fe dopants are uniformly distributed, ranging from diluted ($x \simeq 2-3\%$) up to high ($x \simeq 25\%$) atomic concentration. By x-ray magnetic circular dichroism (XMCD), we carefully analyzed, for samples having different Fe concentration, the magnetic moments as a function of temperature, in the range from 5 K up to 150 K, studying the best dopant concentration range maximizing the magnetic signal. Surprisingly, the iron magnetic moment measured for diluted concentrations degrades as the concentration of magnetic dopant increases. On the basis of ab initio simulations, we propose that the microscopic mechanisms responsible of the peculiar magnetic properties of this compound can be explained by oxygen mediated super-exchange mechanism between the Fe dopants producing, at high dopant concentration, an antiferromagnetic coupling between two Fe atoms. We identify and discuss the role of O vacancies to control such microscopic mechanisms.

Usage: Secondary publications and information retrieval purposes.

PACS numbers: May be entered using the `\pacs{#1}` command.

Structure: You may use the `description` environment to structure your abstract; use the optional argument of the `\item` command to give the category of each item.

I. INTRODUCTION

The synthesis of magnetic semiconductors promises the realization of innovative devices in which the spin of the carriers is exploited as a further degree of freedom in addition to their charge, allowing efficient (and scalable) data storage and transfer [1]. In this context, the availability of room-temperature magnetic semiconductors strongly dictates the possibility to realize commercial spintronic devices that will revolutionize the semiconductor industry in the following years. In the search for room-temperature magnetic semiconductors a significant amount of effort has been dedicated towards the study of Diluted Magnetic Oxides (DMO) [2], i.e. compounds with diluted concentration of magnetic impurities uniformly and randomly distributed in the oxide matrix. In particular, the identification of the microscopic mechanisms responsible for magnetic properties in DMO is of paramount importance because it will pivot the research to novel forthcoming spintronic devices.

Since the prediction that Mn-doped zirconia can support room-temperature ferromagnetism,[3] the attention of material scientists has been focused on magnetically doped zirconia [4–7] and hafnia [8, 9], two similar oxides already extensively studied by the semiconductor industry for their high-dielectric properties [10]. Several works attempted to determine the magnetic nature of transition metal doped zirconia (or hafnia); however, the experimental studies produced contrasting results, suggesting the presence [11–14] or the absence [15] of room-temperature ferromagnetism; furthermore, the magnetic nature of these compounds is still debated (i.e. Ferromagnetic (FM) [16], Antiferromagnetic (AFM) [17], Paramagnetic (PM) [18] or super-PM (SPM)). During the past years, the interpretation of results in the field of diluted magnetic oxides was hindered by some reports about ferromagnetic behavior at room temperature that lately turned out to be originating from spurious signals and artifacts in the measurements (see for example Coey 2006 [19] for a more detailed discussion of this issue).

To avoid possible artifacts encountered with VSM-SQUID magnetometry, we employed state-of-the-art X-ray Magnetic Circular Dichroism (XMCD) to investigate the temperature dependence of the magnetic properties of Fe-doped zirconia, for different dopant concentrations. Our measurements show that at low temperature and diluted concentrations, a magnetic field can induce a big (up to 1.8 μ_B) magnetic moment on the Fe ion while the magnetic moment decreases as the Fe concentration increases. This surprising behavior is

explained, by ab initio simulations, in terms of super-exchange interactions, which, for peculiar Fe configurations at diluted doping, can cause a FM coupling on a finite portion of the crystal, thus producing the detected magnetic moment. At variance, at high doping regime, the super-exchange mechanism produces an AFM coupling between two neighbour Fe dopants substitutional to Zr, mediated by an O in a "bridge" position between the two magnetic impurities.

II. EXPERIMENTAL RESULTS

The samples consist of thin film of Fe-doped fluorite zirconia grown by atomic layer deposition. Fe is uniformly distributed at substitutional Zr sites in the zirconia matrix, as demonstrated in previous publications [20–22]. For overall charge neutrality, the Fe doping induces the formation of O vacancies (V_O), thus forming the compound $Zr_{1-x}Fe_xO_{2-y}$, with y very close to $x/2$ [20], i.e. one V_O every two Fe ($y = x/2$) corresponding to the case with Fe^{3+} oxidation state. In the opposite limiting case of Fe^{2+}, y is expected to be close to x, while intermediate values of y correspond to different Fe^{3+}/Fe^{2+} ratios. The samples were measured at the BESSY synchrotron radiation facility in Berlin, Germany, by X-ray absorption near-edge spectroscopy (XANES) and x-ray magnetic circular dichroism (XMCD) at Fe $L_{2,3}$ and O K edges. The elemental sensitivity of XMCD ensures that the actual magnetic signal is coming from the elements inside the sample, and not from spurious sources such as impurities or the sample holder. Furthermore, elemental sensitivity is useful in the debate around the origin of magnetism in diluted oxides. Indeed it was also proposed that the magnetic moment may reside not only in the dopants [19]. Details of the sample characterization and measurement conditions are reported in the Appendices A and B, respectively.

Figure 1a and 1b show the XANES spectra acquired at O K and Fe $L_{2,3}$ edges for the ZrO_2 samples doped with different concentrations of Fe at 5 K. The O K edge spectra (Fig. 1a) can be subdivided into three main regions. The region I, for energies lower than 531 eV, is characterized by a low intensity peak ascribed to O $2p$ states hybridized with Fe $3d$ states [23, 24], in particular it originates from O atoms with a Fe atom in their first coordination shell [25]. The region II, corresponding to energies in the range of 531-541 eV, shows spectral features mainly due to the transition from the O $1s$ and the O $2p$ state

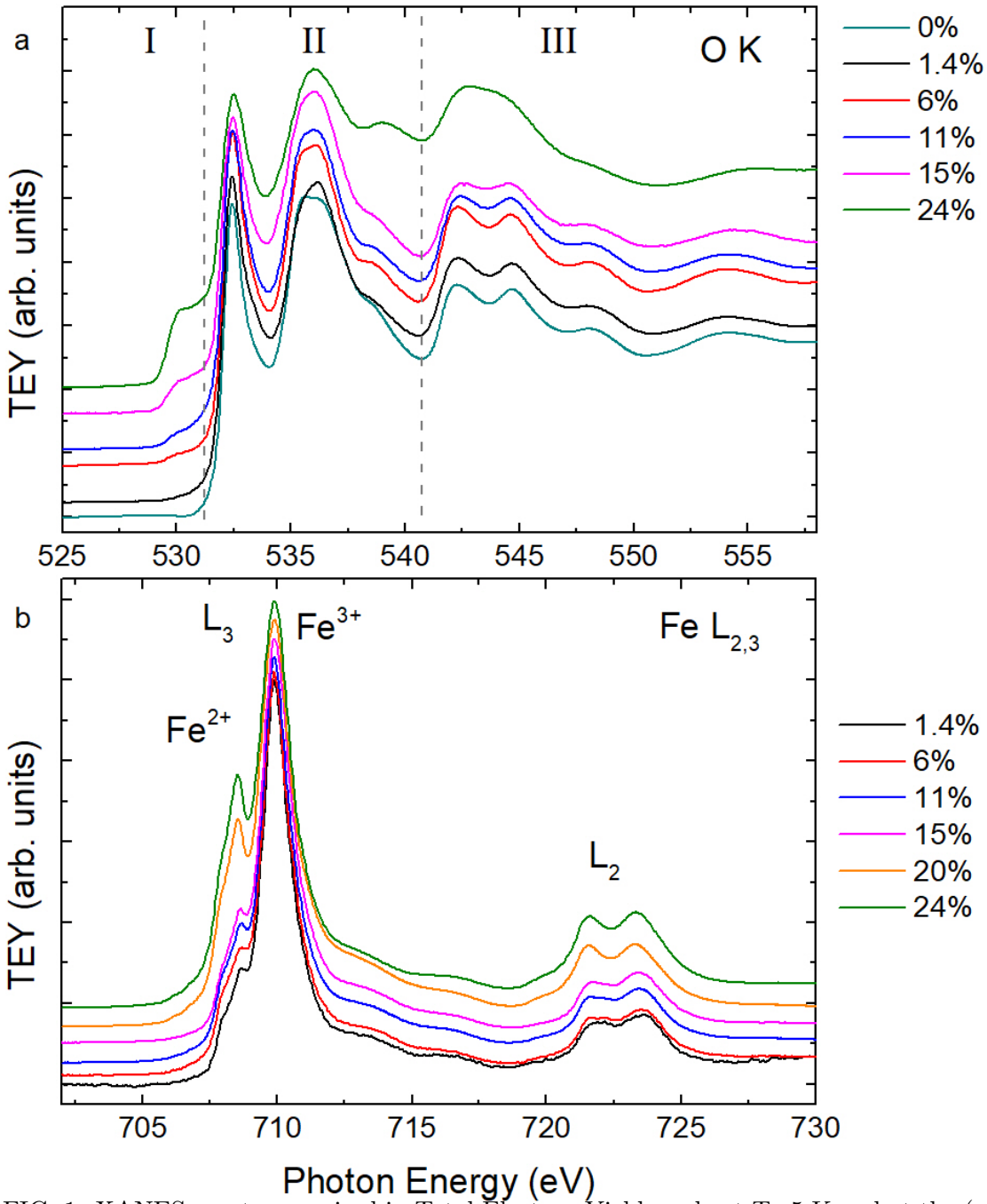

FIG. 1. XANES spectra acquired in Total Electron Yield mode at T=5 K and at the (a) O K and (b) Fe $L_{2,3}$ edges of the ZrO_2 samples doped with different concentrations of Fe.

hybridized with the Zr $4d$ states [26, 27]. The region III, above 541 eV, shows features due to O $2p$ states mixed with Zr $5s$ states. The well resolved shape of the edge-peak ($\sim$ 537 eV) indicates that the samples are crystalline, while the increase in broadness as a function of the dopant concentration is related to the chemical disorder produced by Fe substitutional

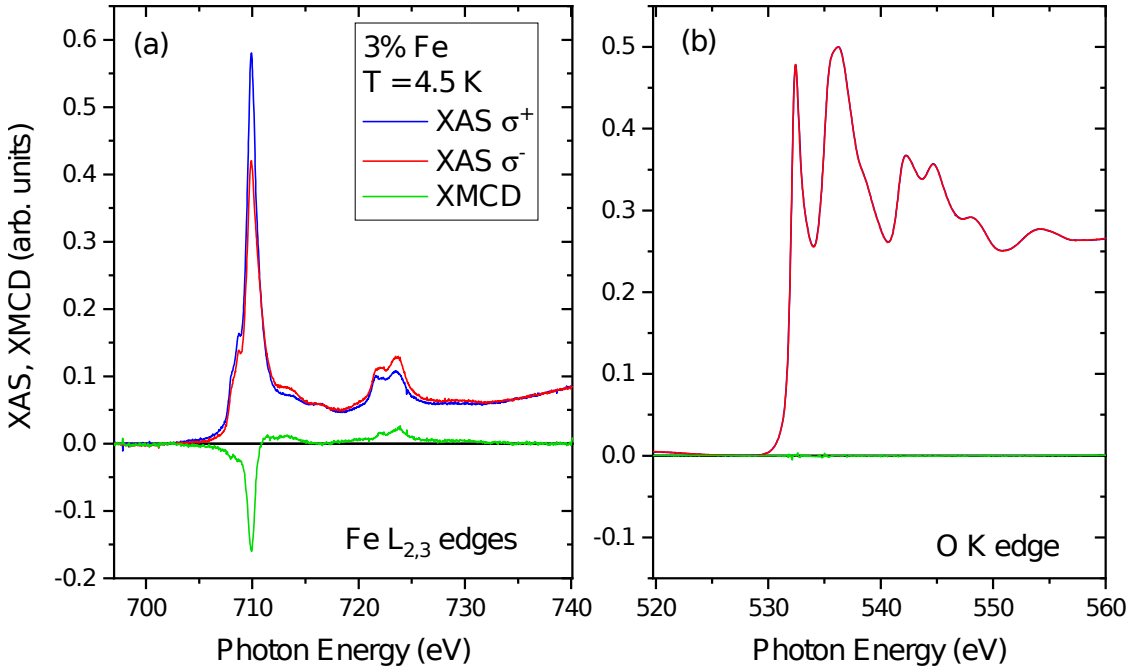

FIG. 2. Absorption spectra taken with opposite photon helicity (red and blue), and corresponding XMCD spectra (green), measured at (a) the Fe L edges and (b) O K edge. These measurements are referred to the sample with 2 % Fe concentration, at 4.5 K with an applied field of 6 T. The lineshape is representative for all the samples. The spectra were rescaled so that the isotropic XAS spectra (the sum of left- and right-circularly polarized spectra, not shown in the figure) is normalized between 0 and 1.

impurities randomly distributed at the Zr sublattice sites [25, 27, 28].

The Fe $L_{2,3}$ spectra (Fig. 1b) are due to transitions from $2p$ core level into empty $3d$ states of Fe in the presence of a crystal field [29]. The presence of localized states both at L_3 and L_2 reveals a mixture of Fe^{2+} and Fe^{3+} states (see for example references [30, 31]). This can be stated by a comparison with crystal-field multiplet calculations, which predict a shift in the main peak for different valence states of Fe (irregardless of the crystal field symmetry) [32]. Unfortunately, the energy separation of the main peak between Fe^{3+} and Fe^{2+} is closely matching the crystal field splitting for Fe_2O_3, so the presence of such a phase on the local scale cannot be ruled out completely. Following our main interpretation, for Fe concentration < 15 at.% the 3+ valence of Fe is the largely predominant oxidation state (Fig. 3a), however for higher dopant concentration, the Fe^{3+}/Fe^{2+} ratio drops. Indeed, the pre-edge peak ($\sim$ 708.7 eV) increases in sharpness and intensity (Fig. 1b) indicating

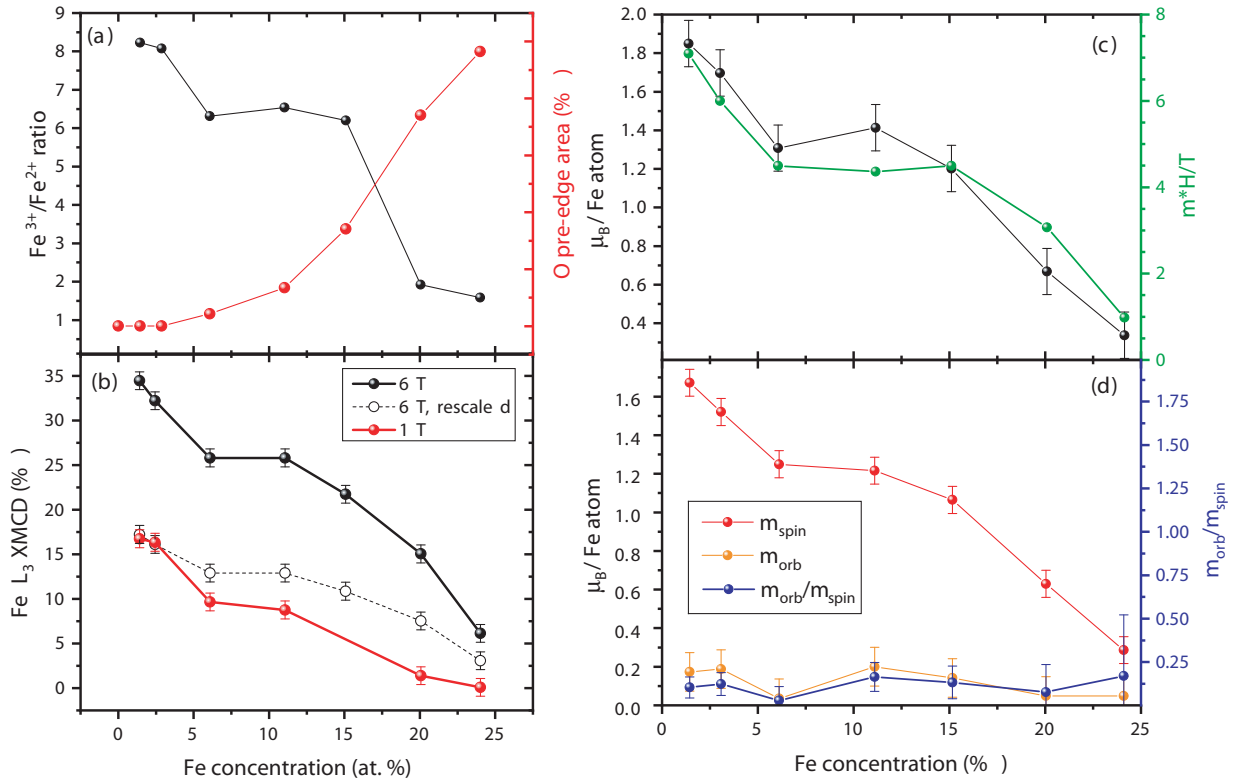

FIG. 3. (a) the Fe^{3+}/Fe^{2+} ratio and the O pre-edge peak area [from A. Lamperti *et al.* J. Vac. Sci. Technol. A **36**, 02D404 (2018)] and (b) the Fe L_3 XMCD signal as a function the dopant concentration. T=5 K. (c) Comparison of the trend of m_{tot} obtained by applying the sum rule analysis to the XANES spectra and $(\mu H)/T$ obtained by fitting the Fe L_3 XMCD signal as a function of the temperature with a Langevin function and (d) m_{orb}, m_{spin} and m_{orb}/m_{spin} ratio as a function of the dopant concentration.

a significant increases in the amount of Fe^{2+}. Since Fe replaces a Zr^{4+} atom, the increase in Fe^{2+} sites can be related to a significant increase in the amount of O vacancies (i.e. in $Zr_{1-x}Fe_xO_{2-y}$, y grows from $x/2$ towards x). From the O K edge spectra, the drop of the Fe^{3+}/Fe^{2+} ratio happens to be correlated by a steep increase in the intensity of the O pre-edge peak at about 530 eV (Fig. 3a) and to a decrease in intensity of the peak at 537 eV [25]

No magnetic contrast was found at the O K and Zr $L_{2,3}$ edges, while a very strong signal was found at the Fe $L_{2,3}$ edges. A representative example is shown in figure 2. In particular, the highest XMCD signal was found for the lowest dopant concentration, and it decreases monotonically for higher content of Fe. At 24 at. % doping, it is almost zero (Fig. 3b).

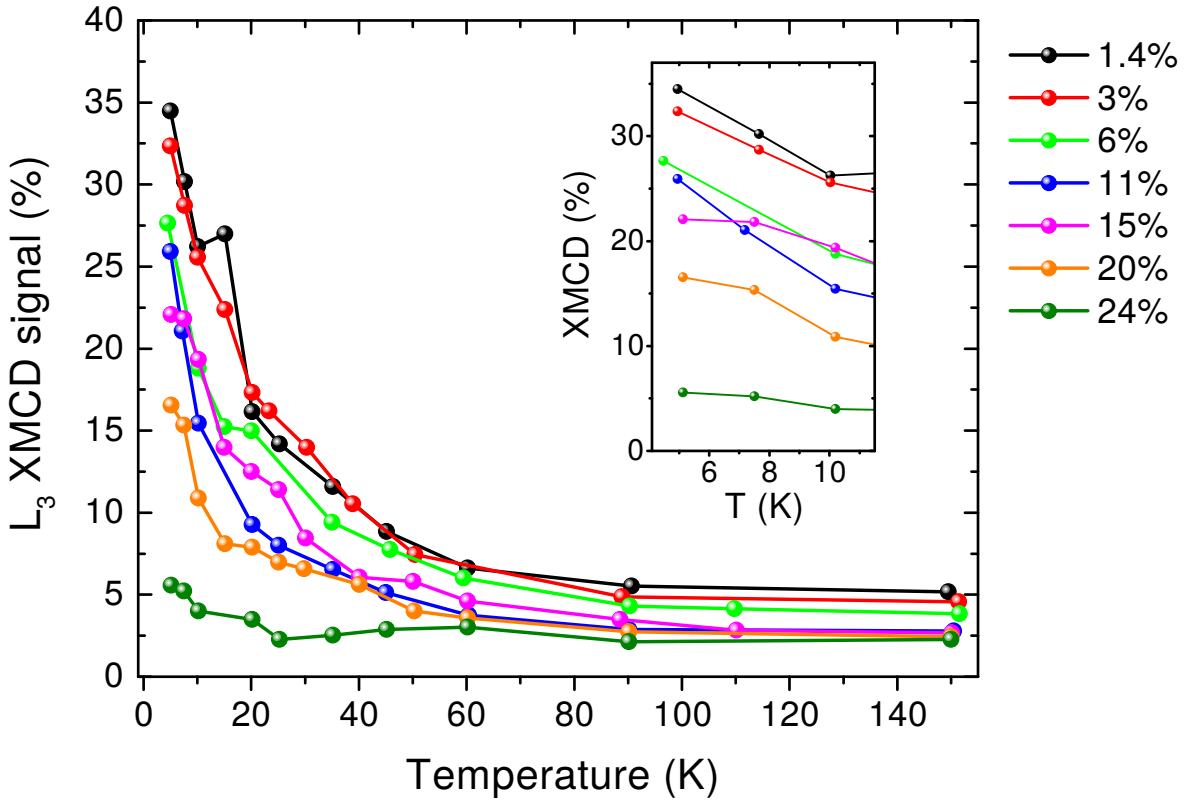

FIG. 4. Fe L_3 XMCD signal, for the investigated Fe concentrations, as a function of the temperature. The external magnetic field is equal to 6 T.

This signal reduction is in agreement with the increase in the amount of Fe^{2+} (having a smaller magnetic moment than Fe^{3+}) in the highly-doped samples. However, the observed decrease of the XMCD signal cannot be explained only by the difference in the Fe^{3+}/Fe^{2+} ratio. Supposing that the magnetic moment of Fe^{2+} is about 4/5 the one of Fe^{3+}, a change in the ratio from 8.5 to 2 (as quantified in Fig. 3a for samples doped with 1 and 24 at. %, respectively) would produce a variation of the total magnetic moment by less than 10%. Instead, the most diluted sample has a signal more than three times bigger than the one with the highest doping level. This suggests that a significant change in the magnetic interaction between the Fe atoms should happen with varying concentration. A mechanism to explain this aspect is proposed in the next section.

While the spectral features of the XANES spectra are completely unaffected by the increase in the measuring temperature, the XMCD signal strongly changes. Figure 4 shows the behavior of the XMCD signal at the Fe L_3 edge as a function of the measuring temperature for the different samples. The XMCD signal asymptotically decreases with temperature

to reach almost zero for temperatures higher than 50 K. Comparing different samples, we observe a slightly different behavior in the low-temperature dependence of the XMCD signal. For concentrations up to 11%, the measured XMCD increases almost linearly between 10 and 4.5 K. Instead, in samples doped with 15-24 at.% this increase is less pronounced and resembles a saturation of the magnetic signal below 10 K. This is shown in the inset of Fig. 4. This may be a symptom of antiferromagnetic coupling between Fe atoms, in accordance with the simulations presented in the next section. Frustrated magnetic interactions due to disorder or competing FM/AFM coupling may also be at the origin of the observed behavior.

The results obtained by fitting XMCD vs. T curves with a Langevin function are summarized in Fig. 3c and are in good agreement with those obtained by applying the sum rules analysis to the XANES/XMCD spectra (Fig. 3d). m_{spin} and m_{orb} are parallel (Fig. 3d), the m_{orb}/m_{spin} ratio is dominated by m_{orb}, while the total magnetic moment ($m_{tot} = m_{spin} + m_{orb}$) (Fig. 3c) is governed by m_{spin}. m_{orb} is almost constant for all Fe dopant concentrations, while both m_{spin} and m_{tot} decrease showing a plateau for Fe concentration in the 6-15 at.% range.

It is interesting to notice that the highest magnetic moment measured is actually close in magnitude with that of metallic iron (which is 2.2 μ_B). In paramagnetism, the magnetic behavior is determined by the ratio $\mu H/k_B T$ (the argument of the Langevin function in the classical model of paramagnetism). For a magnetic moment of 1 or 2 Bohr magnetons, with a field of 6 T and at 5 K, the ratio would be still below 2. In these conditions, thermal agitation is still significant and the average magnetization should be less than half of its saturated value. Moreover, the magnetization should be linearly dependent from the applied field. The high magnetic response measured suggests that the system shows a high susceptibility and/or a high magnetic moment, not expected for a typical paramagnet. Further, if we compare the data measured at 6 T and 1 T in Fig. 3b we see that the two data sets do not differ by just a multiplicative factor (see Fig. 3b, data at H=6 T rescaled). This is a hint of the fact that at low doping concentration, the system may be in a regime in which the M(H) relationship is not linear, i.e. the system is somehow closer to the saturation regime. This is something usually observed in super-PM systems, due to the fact that the "elementary" magnetic moments that behave paramagnetically are very big, since they originate from a large ensemble of interacting atoms. Hence in super-PM systems the susceptibility is usually

big and the system can be saturated at reasonable fields.

III. COMPUTATIONAL RESULTS

To identify the microscopic mechanisms responsible for magnetic coupling in Fe-doped ZrO_2, we performed first principles simulations by plane-wave pseudopotential techniques of $Zr_{1-x}Fe_xO_{2-y}$, with $x = 6.25$ at. %, a concentration where both FM coupling (at diluted doping) and mechanisms responsible for the degradation of FM coupling (at moderate/high doping) are expected according to the experimental data. We used a 95 atoms super-cell of ZrO_2 containing two Fe and one O vacancy (V_O), which is located in the nearest neighbour (NN) O-shell of one substitutional Fe to Zr, denoted as Fe_1, while the position of the other Fe atom, Fe_2, varies over all substitutional Zr sites of the super-cell. After atomic relaxation, the V_O migrates in the next NN O-shell to Fe_1, so Fe_1 in the relaxed structure has a NN shell composed of four O and has a V_O in the next NN O-shell that is composed of three O. At variance, the Fe_2 is at the center of two neighbour (NN and next NN) O-shells composed of four O each, which is also the shell structure of O surrounding the Zr in fluorite zirconia. In the simulations, the number of O atoms in a given shell can be un-ambiguously determined, and by comparison with the bulk case (without vacancies) the number of O vacancy in one shell can be easily computed. At variance, the assignment of an exact position to the O vacancy in that shell can be questionable (since, in general, none of the O present in the shell with a O vacancy has conserved its original bulk position). For this reason, we do not indicate a position of an O vacancy in right panel of Figs.6,8 – where we display the relaxed atomic structure for two different Fe-Fe configurations – but rather we limited the discussion of the position and the role of O vacancies in the text.

For each atomic configuration (Fe_1,Fe_2) we computed the total energy of both the FM (E_{FM}^{TOT}) and AFM (E_{AFM}^{TOT}) relaxed structures. The difference, that to a first approximation can be considered proportional to the exchange coupling parameter $J \propto \Delta E_J \equiv E_{AFM}^{TOT} - E_{FM}^{TOT}$, is a function of the Fe-Fe distance and of the angle formed by Fe_2 with the Fe_1-V_O complex. In the following discussion, we will ignore the O sublattice and consider only the Zr sublattice in which the Fe are substitutional to Zr sites arranged according to the pristine fluorite structure, that is taken as a reference to determine the partition into shell and also the distance (reported in Fig. 5) from an atom (Fe_2) in a given shell to the central

atom (Fe_1) [33]. In the chosen super-cell, Fe_1 is surrounded by 5 Zr-shells at increasing distance from the central Fe_1. Fe_2 is placed in one substitutional site of the *n-th* shell (with *n=1,2,3,4,5*). For each shell we averaged $E^{TOT}_{AFM} - E^{TOT}_{FM}$ over all the Fe_2 configurations; in Fig. 5, we display our results for the mean and the standard deviation as a function of the Fe_1-Fe_2 distance.

When Fe_2 is placed in the first nearest-neighbour (NN) Zr-shell to Fe_1, the magnitude and the sign of the exchange interaction varies significantly among all distinct 12 configurations, from FM to AFM coupling, due to the presence of V_O close to both Fe atoms, thus producing a large standard deviation. The atomic configuration of the ground state, in which Fe_1 and Fe_2 are NNs in Zr-lattice is displayed in Fig.6 and presents a significant AFM coupling of the two Fe with $\Delta E_J = -105$ meV.

Among all possible Fe_1-Fe_2 configurations allowed by the super-cell size, the more energetically favored FM state has an energy 0.15 eV higher than that of the ground state, corresponding to the configuration we denoted as FAR, in which Fe_2 is placed in the farthest shell of the super-cell, i.e. the distance between each Fe and its nearest Fe is the maximum allowed by an uniform dopant distribution with x=6.25 at. %.

For Fe_2 in the intermediate shells (n=2,3,4), ΔE_J, proportional to the exchange interaction, is very small, of the order of a few meV, thus providing a PM contribution, and does not vary significantly within the same shell among the different Fe_2 configurations.

The magnetism is thus determined by two competing mechanisms: the AFM coupling when two substitutional Fe are NNs in the Zr-sublattice, and the FM coupling when two substitutional Fe are far apart.

A. The AntiFerromagnetic ground state

At first, we analyze the AFM ground state, having Fe_2 positioned in the first Zr-shell to Fe_1. Since, according to our analysis, the main contribution to magnetization relies on Fe *d*-orbitals and O *p*-orbitals, in the following discussion and in scheme of the magnetic interaction (Fig. 7) we refer to these orbitals only, while minor contributions from *s*-states are neglected.

The relaxed atomic configuration of the AFM ground states is displayed in Fig. 6. After atomic relaxation each Fe is surrounded by a shell of four O atoms, one of these oxygens,

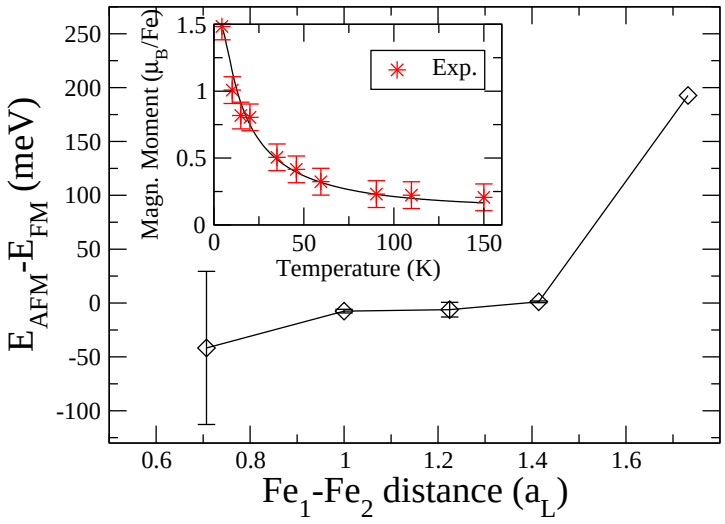

FIG. 5. First principles simulation of $Zr_{1-x}Fe_xO_{2-x/2}$ with $x = 0.0625$. Shell average (mean and standard deviation) of the energy difference between fully relaxed AFM and FM spin configurations. The shell structure is defined according to Zr sublattice of bulk ZrO_2 fluorite, that is also used to express the distance (in crystal units a_L) of a shell from the central atom. Insert: magnetic moment (in Bohr magneton) per Fe atom as a function of temperature obtained by solving a mean filed model (solid black line) and by applying the sum rule analysis to the XANES spectra (red stars)

denoted as O_{bridge}, is shared by the two shell resulting in a "bridge" position between the

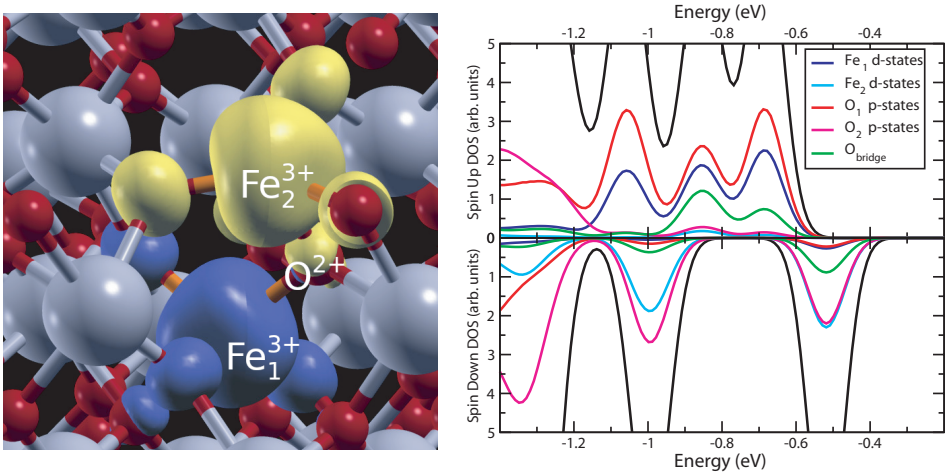

FIG. 6. Left Panel: The atomic configuration of the antiferromagnetic ground state of $Zr_{1-x}Fe_xO_{2-x/2}$ with $x = 0.0625$. The symbol O^{2+} labels the O in *bridge* position between two Fe. The isosurface (at 0.007 a.u.$^{-3}$ corresponding to $\sim 1\%$ of the maximum of the valence spin-density) for the spin-up (yellow) and spin-down (blue) density of states is also displayed. Right Panel: The corresponding Total (black solid line) and Projected (colored solid line) Density of States, normalized to the super-cell. The zero of the energy scale corresponds to the Fermi energy.

two Fe. The angle θ formed by the Fe_1-O_{bridge}-Fe_2 bonds is $\theta = 112°$, compatible with an AFM coupling that is proportional to $[cos(\theta)]^2$ [34]. The AFM coupling is due to the super-exchange interaction among the spin polarized d-states of Fe, mediated by the p-orbital of the O_{bridge}. The scheme for O-mediated super-exchange interaction among two Fe is displayed in Fig. 7; the Fe_1-O_{bridge}-Fe_2 structure reproduces the standard scheme coupling two Fe^{3+} [34, 35]. It is worth to notice that, as a result of the difference in the oxidation state of the Zr and its substitutional Fe, the four O surrounding the Fe are partially polarized, as can be noticed in Fig. 6 (left panel) looking to the isosurface of the spin polarized valence electron density. The O_{bridge} participates to the exchange interaction, and its magnetic moment (obtained by projecting the spin resolved electron valence density on atomic orbitals) basically vanishes ($\sim 0.08\ \mu_B$), while the other three O of each NN shell present a small spin polarization ($\sim 0.2\ \mu_B$), due to hybridization of the O (mainly p) and Fe (mainly d) valence states; the spin polarization of these O is the same of the Fe they surround, and is due to a partial charge transfer from O p-orbitals to Fe d-orbitals. The charge transfer involves the nearest neighbour O to each Fe resulting in global transfer of one electron to the Fe d-orbital and

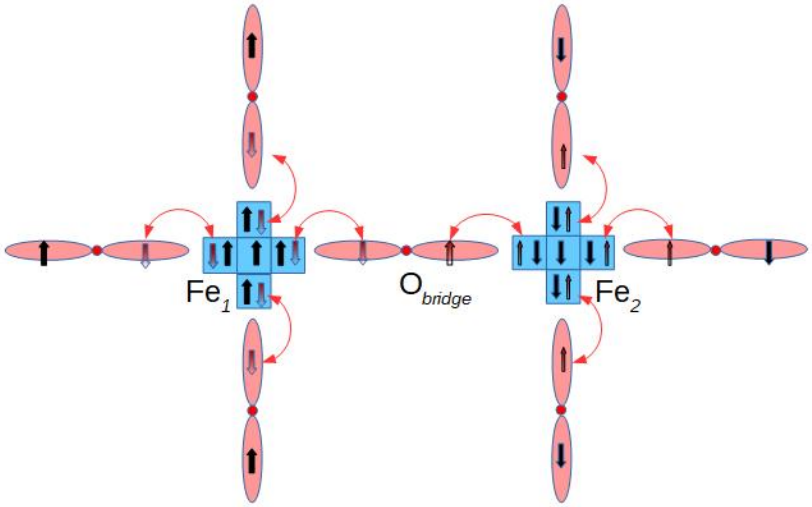

FIG. 7. The super-exchange scheme of antiferromagnetic coupling. Light blue denotes Fe orbitals (squares: *d*-states). Light red denotes O orbitals (double ellipses: *p*-states). A red line connects the same spin-polarized electron (denoted by shadow red arrow) occupying a hybrid bond shared by two nearest neighbour atoms.

the consequent partial polarization of the *p*-states of the surrounding O, according to the Hund's rule applied to the hybrid *pd*-orbitals. The scheme is illustrated by the six O (three O for each Fe) not in the *bridge* position in Fig. 7. Since this charge transfer mechanism (due to hybridization) does not change the overall magnetization of the Fe and its nearest-neighbour O, the Fe can still be considered in the Fe^{3+} oxidation state with the advice that the corresponding five spin polarized electrons now occupy five hybrid *pd* orbitals (O-*p* and Fe-*d* states) instead of the usual five Fe *d*-orbitals.

This super-exchange interaction is clearly shown in the projected density of states (DOS) displayed in Fig. 6 (right panel) where is reported the energy range corresponding to the upper part of the valence bands (a more complete plot of the projected DOS is reported in Appendix C.2). The structure at energy lower that -1.2 eV originates from the electronic valence states of zirconia, while the peak structure at higher energy (from -1.2 eV up to -0.4 eV) represents the occupied electronic states in the bandgap of (undoped) zirconia, and are due to the interaction of each Fe with its four nearest neighbour O, producing the above mentioned orbital hybridization. By looking to the spin up DOS of Fig. 6 (right panel), in the energy range from -1.2 eV to -0.6 eV, the three peaks produced by the *p*-

orbitals (red line) of the three O (denoted as O_1, with $O_1 \neq O_{bridge}$) surrounding Fe_1 are superimposed to the corresponding peaks produced by the *d* orbitals of Fe_1 (blue line), resulting an hybridization of *pd*-orbitals at the same energy. In a similar way, by looking to the spin down DOS of Fig. 6 (right panel), in the energy range from -1.1 eV to -0.4 eV, the two peaks produced by the *p*-orbitals (magenta line) of the three O (denoted as O_2, with $O_2 \neq O_{bridge}$) surrounding Fe_2 are superimposed to the corresponding peaks produced by the *d* orbitals of Fe_2, resulting in a hybridization of *pd*-orbitals at the same energy, as well. In the energy range under consideration, the *p*-orbital DOS of O_{bridge} (green line) presents: i) two peaks in the spin-up DOS that are superimposed to the two peaks (at about -0.85 eV and -0.68 eV) corresponding to the *pd*-orbitals of O_1 and Fe_1, ii) two peaks in the spin-down DOS that are superimposed to the two peaks (at about -1.00 eV and -0.52 eV) corresponding to the *pd*-orbitals of O_2 and Fe_2. The asymmetry in the spin-up and spin-down DOS as well as the presence of a very small magnetization of the O_{bridge} can be attributed, at least in part, to the asymmetry in the coupling due to the presence of a O vacancy. The presence of both spin-up and spin-down peaks in the *p*-DOS of O_{bridge} couples AFM the two Fe (and other nearest neighbour O of each Fe, trough hybrid orbitals), enlightening the microscopic mechanism responsible of AFM coupling produced by the super-exchange interaction.

B. The Ferromagnetic state for Fe uniform distribution

Now we analyze the FM coupling of the FAR configuration, where the two Fe are placed at the maximum relative distance compatible with periodic boundary conditions, thus corresponding to the configuration in which the Fe are uniformly distributed in the super-cell (or in the whole crystal).

The relaxed atomic configuration of the FM ground states is displayed in Fig. 8 (left panel). After atomic relaxation, each Fe is surrounded by a NN shell of four O atoms that are partially polarized, as can be noticed by looking to the isosurface of the spin polarized valence electron density displayed in Fig. 8.

We propose that FM coupling of the two Fe can be explained by a super-exchange-like mechanism [35] by considering the hybridization of Fe *d* and *s*-orbitals with *sp*-orbitals of the four O NNs to the Fe.

This hybridization produces semi-covalent oriented bonds that are filled according to the

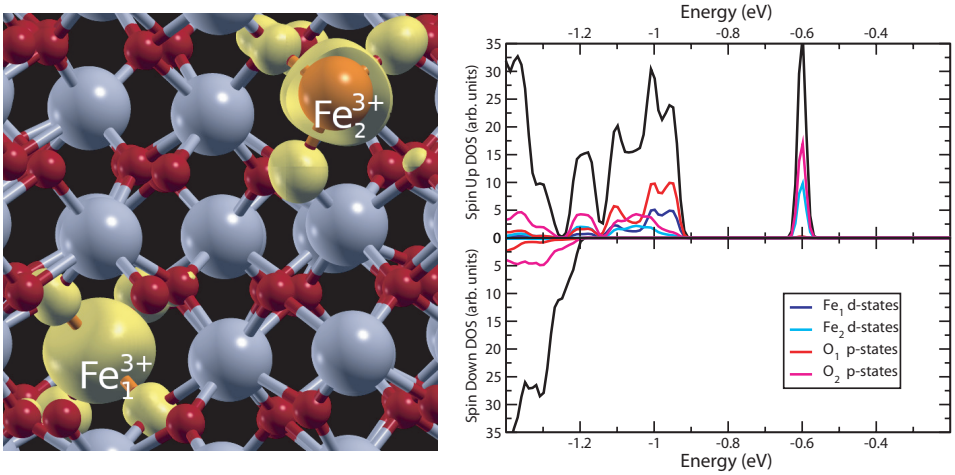

FIG. 8. Left Panel: The atomic configuration of the ferromagnetic state with lower energy of $Zr_{1-x}Fe_xO_{2-x/2}$ with $x = 0.0625$. The isosurface (at 0.007 a.u.$^{-3}$ corresponding to $\sim 1\%$ of the maximum of the valence spin-density) for the spin-up (yellow) density of states is also displayed. Right Panel: The corresponding Total (black solid line) and Projected (colored line) Density of States, normalized to the super-cell. The zero of the energy scale corresponds to the Fermi energy.

Hund's rule. Since some bonds participating to hybridization are empty, an electron with the same spin-orientation of Fe magnetic moment occupies the hybrid-orbitals formed by Fe and its 4-NNs O, resulting in a polarized bond oriented according to the local disposition of NN-O surrounding the Fe. The FM interaction is mediated by O through super-exchange mechanisms. An illustrative scheme is displayed in Fig. 9, where the top left Fe (Fe_1) presents a semi-empty hybrid bond (of $4s$ nature) partially occupied by a spin-up electron shared with the *sp* orbital of NN O, according to the super-exchange mechanism described above (see also Appendix C.2). This spin polarization of the O bonds can propagate through the crystal by means of the *sp*-orbitals of other O, the latter orbitals do not present a net magnetic moment, but rather a "spatial" polarization of orbitals of opposite spin (represented by the O with two black arrows in the middle of Fig. 9 and labeled as O^{2-}) caused by the partial hybridization with *sp*-orbital of O that are NN to the Fe. If one of the ("propagated") polarized O-bonds hybridizes with the *d*-orbitals of an other Fe (Fe_2), a FM coupling between the two Fe occurs.

The FM coupling of *d*-states of each Fe with *p*-states of its NN-O is visible in the projected DOS in Fig. 8, where the contribution to the DOS originated from the orbitals forming hybrid semi-covalent bonds are superimposed at the same energy, while for the role played

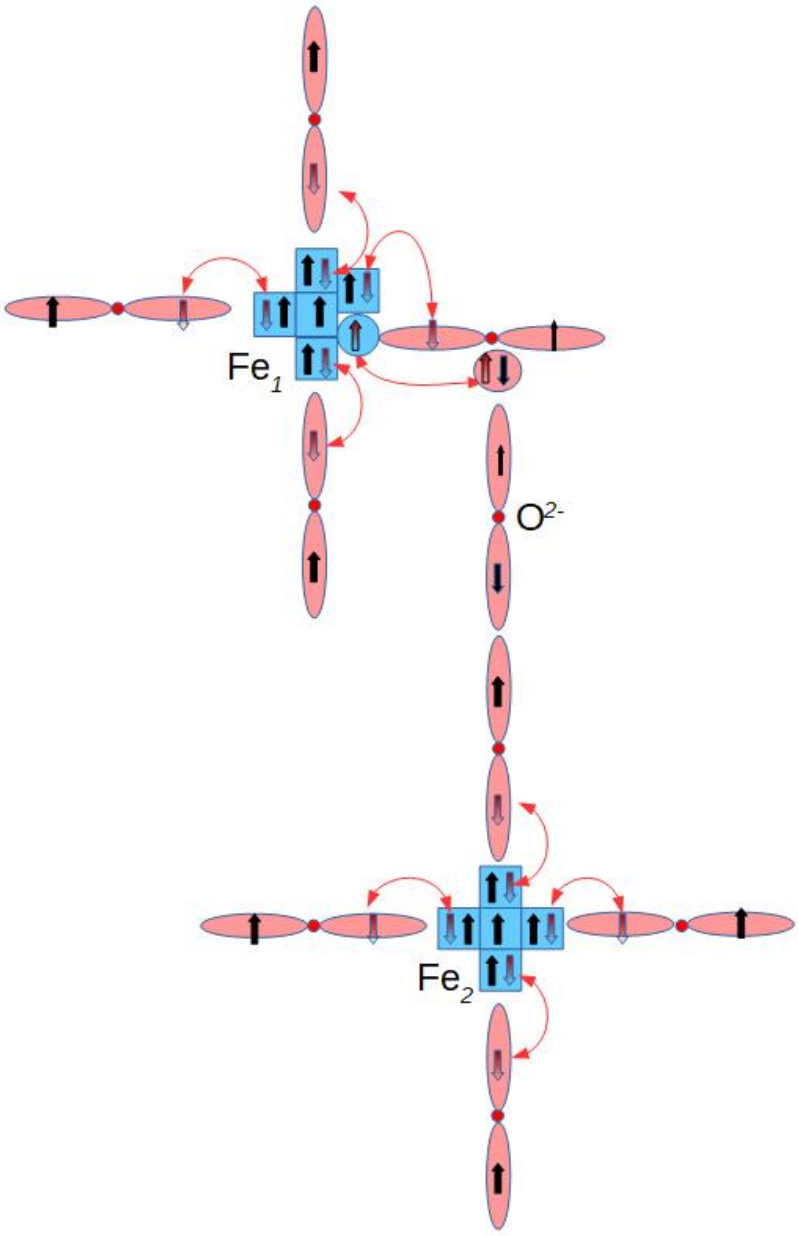

FIG. 9. The super-exchange scheme of ferromagnetic coupling. Light blue denotes Fe orbitals (squares: *d*-states; circle: *s*-states). Light red denotes O orbitals (double ellipses: *p*-states; circle: *s*-states). A red line connects the same spin-polarized electron (denoted by shadow red arrow) occupying a hybrid bond shared by two nearest neighbour atoms.

by *s*-orbitals the reader can refer to Appendix C.2. In the right panel of Fig. 8, O_1 and O_2 denotes the sum of *p*-orbitals DOS of the four O in the NN shell to Fe_1 and Fe_2, respectively. In the energy range from -1.2 eV to -0.9 eV, the Fe_1 *d*-states (blue line) can hybridize with

the O_1 p-states (red line) at the same energy, the same is true also for Fe_2 d-states (turquoise line) and O_2 p-states (magenta line). Further, the O in the next NN shell to Fe_1 and Fe_2 have a similar, but smaller, p-DOS structure in this energy range as the O in the NN shell. As a result, the polarization of O p-orbitals induces a FM coupling between the two Fe. As a fingerprint of the asymmetric coupling between Fe_1 and Fe_2 (Fig. 9) we notice that the polarization, originated also by the presence of Fe_1-V_O complex, blue-shifts the semi-covalent bonds formed by Fe_2 with its NN-O (turquoise and magenta peaks at -0.6 eV in Fig. 8) at an energy higher that the one of the corresponding peak of semi-covalent bonds formed by Fe_1 with its NN-O (blue and red peaks at -1.0 eV in Fig. 8).

Incidentally, the presence of space-oriented hybrid bonds also explains the large standard deviation of ΔE_J in Fig. 5 for the first shell.

IV. DISCUSSION

In light of the theoretical results, we propose that the measured magnetic behaviors can be explained, at least qualitatively, as follows. The chemical disorder, due to the random Fe distribution in Zr-sublattice, produces fluctuations of the Fe-Fe distance. So, for a random distribution of Fe in the Zr sub-lattice the PM, FM, and AFM interactions can coexist according to the different mutual Fe distances and arrangements. In general, if two (or few) Fe are FM coupled but their coupling with surrounding Fe is of PM nature, the system macroscopically behaves like a paramagnet [36]. A FM order, possible only assuming that a FAR configuration is extended on a macroscopic scale, has a statistically vanishing probability to be realized, due to random distribution of Fe. Furthermore, for a given concentration of randomly distributed Fe, the different magnetic couplings, due to the different Fe-Fe distances and arrangements, produce, also at low temperature, an average Fe magnetic moment (defined as the total magnetic moment divided by the number of Fe) that is only a fraction of the magnetic moment of a single Fe, due to the presence of some AFM coupled Fe. Since the arrangements of Fe atoms creating a configuration similar to the FAR one are statistically possible only with configurations involving few Fe couples FM-ordered in limited-size regions of the sample, the formation of a long range magnetic order is prevented, but the system is paramagnetic and magnetically polarizable with a high magnetic moment per atom. Regions of the sample in which a FAR-like configuration is statistically generated

by the random distribution of Fe can eventually develop FM ordering at the nanometer scale, typical of super-paramagnetism. The similarity with super-PM systems should be investigated further with dedicated experiments. An hysteresis loop with finite coercivity should be detectable below the blocking temperature. Susceptibility measurements as a function of temperature should display significant differences in the Curie constant for samples which are simply PM and samples in which super-PM behaviors are present, due to the difference in magnitude of the "effective" magnetic moments.

To verify that the mechanism proposed from first principles simulations is compatible with the experimentally observed behavior, we can compare the Fe L_3 XMCD signal for x=6 at.% at H=6 T, shown in Fig. 4, with the corresponding theoretical magnetization as a function of temperature, displayed in the insert of Fig. 5, which has been computed, from our ab initio data for $x = 6.25$ at.%, by solving a mean field model with an external magnetic field of 6 T. As ingredients of the mean field model we used the exchange coupling coefficients estimated by the total energy approach, where the energy difference of the FM and AFM states are determined by our first principles results. There are more sophisticated techniques to extract the exchange coupling coefficients, they are based on linear response [37] or frozen magnons [38]. However, such approaches – usually used to compute the critical Neél or the Curie temperature [39, 40] – are beyond the scope of the present work aimed to determine the magnetic interaction at low temperature. To compute the trends of the magnetization as a function of temperature, the total energy approach adopted here is sufficient to bring out the principal features of the magnetic interaction in DMO as previously reported in literature [39–41].

As can be noticed from Fig.s 4 and 5, experimental and theoretical data show very similar behaviors. In spite of the simple model used (details in Appendix C.3), the computed average magnetization of 1.45 μ_B per Fe atom at a temperature of 5 K and an external magnetic field of 6 T, is in more than satisfactory agreement with the experimental value of 1.3 μ_B (displayed in Fig. 3d).

The AFM super-exchange mechanism is responsible for the decrease in the magnetic signal as the Fe concentration increases, as shown in Fig. 3b (see also c,d). In fact, for a uniform dopant distribution, the increase of Fe concentration produces a decrease of the average distance between two neighbour Fe. In particular, when the concentration is so large as to produce a significant probability to have two Fe in NN position in the Zr-sublattice, we expect

a significant reduction in the magnetic signal. Assuming a uniform random distribution of Fe substitutional to Zr-sublattice, the critical site percolation concentration is $x_c \simeq 0.2$, [42] i.e. for this and for higher Fe concentration, the crystal is in an AFM state. In fact, if we imagine a "link" connecting two AFM coupled Fe placed in NN sites of Zr-sublattice, then for $x > x_c$ the whole crystal can be imagined connected by a (figurative) "chain" composed of such links, producing an AFM. Significantly, for the sample with 24 at. % –thus having a concentration above the percolation threshold– the experimental magnetization practically vanishes suggesting the possibility of a transition to a fully AFM phase.

V. CONCLUSION

By combining synchrotron data and ab initio simulations, we identified the bond-oriented super-exchange mechanism as the responsible for the peculiar magnetic properties at low temperature in Fe-doped ZrO_2, producing paramagnetic interaction at diluted concentration. On the contrary, as the Fe concentration increases, the magnetic signal decreases, due to the O-mediated super-exchange AFM interaction, which prevails for a high Fe concentration in the range of 18-25 at.% i.e., a concentration at which a significant amount of Fe impurities, substitutional to Zr, are expected to interact through the super-exchange mechanism mediated by an O located in a bridge position (Fe-O-Fe) between two neighbor Fe atoms.

ACKNOWLEDGMENTS

Synchrotron radiation data were obtained at Helmholtz- Zentrum Berlin für Materialien und Energie (BESSY II) under Project No.16204394. Samples were obtained within the framework of project OSEA (No. 2009-2552), financed by the CARIPLO foundation. We acknowledge CINECA for computer resources allocated under ISCRA initiative (AIXAS), and R. Colnaghi for technical support on computer hardware.

[1] T. Dietl and H. Ohno, Rev. Mod. Phys. **86**, 187 (2014).

[2] S. Pearton, W. Heo, M. Ivill, D. Norton, and T. Steiner, Semicond. Sci. Technol. **19**, R59–R74 (2004).

[3] S. Ostanin, A. Ernst, L. M. Sandratskii, P. Bruno, M. Däne, I. D. Hughes, J. B. Staunton, W. Hergert, I. Mertig, and J. Kudrnovský, Phys. Rev. Lett. **98**, 016101 (2007).

[4] I. Zhitomirsky, M. Niewczas, and A. Petric, Mater. Manuf. Process. **18**, 719–730 (2003).

[5] J. Zippel, M. Lorenz, A. Setzer, G. Wagner, N. Sobolev, P. Esquinazi, and M. Grundmann, Phys. Rev. B **82**, 125209 (2010).

[6] X. Zhao, M. Wang, T. Wei, J. Ren, W. B., Y. Han, and Z. Zhao, J. Supercond. Nov. Magn **31**, 2559–2565 (2018).

[7] P. Pramanik, S. Singh, D. C. Joshi, A. Mallick, K. Pisane, A. H. Romero, S. Thota, and M. Seehra, J. Phys. D-Appl. Phys. **51**, 225304 (2018).

[8] N. H. Hong, N. Poirot, and J. Sakai, Appl. Phys. Lett. **89**, 042503 (2006).

[9] K. K. Bharathi, S. Venkatesh, G. Prathiba, N. H. Kumar, and C. V. Ramana, J. Appl. Phys. **109**, 07C318 (2011).

[10] J. E. Jaffe, R. A. Bachorz, and M. Gutowski, Phys. Rev. B **72**, 144107 (2005).

[11] N. H. Hong, C.-K. Park, A. T. Raghavender, O. Ciftja, N. S. Bingham, M. H. Phan, and H. Srikanth, J. Appl. Phys. **111**, 07C302 (2012).

[12] N. H. Hong, M. B. Kanoun, S. Goumri-Said, J.-H. Song, E. Chikoidze, Y. Dumont, A. Ruyter, and M. Kurisu, J. Phys.-Condes. Matter **25**, 436003 (2013).

[13] S. Kumar and A. K. Ojha, Mater. Chem. Phys. **169**, 13 (2016).

[14] K. Kalam, H. Seemen, P. Ritslaid, M. Rähn, A. Tamm, K. Kukli, A. Kasikov, J. Link, R. Stern, S. Dueñas, H. Castán, and H. García, Beilstein J. Nanotechnol. **9**, 119 (2018).

[15] S. Kumar, S. Bhunia, J. Singh, and A. K. Ojha, J. Alloy. Compd. **649**, 348 (2015).

[16] T. R. Sahoo, S. S. Manoharan, S. Kurian, and N. S. Gajbhiye, Hyperfine Interact. **188**, 43 (2009).

[17] I. Kuryliszyn-Kudelska, A. Arciszewska, M. Małolepszy, M. Mazurkiewicz, L. Stobinski, A. Grabias, M. Kopcewicz, W. Paszkowicz, R. Minikaev, V. Domukhovski, N. Nedelko, and W. Dobrowolski, J. Alloy. Compd **632**, 609 (2015).

[18] A. de Souza, F. F. Ivashita, V. Biondo, A. Paesano, and D. H. Mosca, J. Alloy. Compd. **680**, 701 (2016).

[19] J. M. Coey, Current Opinion in Solid State and Materials Science **10**, 83 (2006).

[20] D. Sangalli, A. Lamperti, E. Cianci, R. Ciprian, M. Perego, and A. Debernardi, Phys. Rev. B **87**, 085206 (2013).

[21] D. Sangalli, E. Cianci, A. Lamperti, R. Ciprian, F. Albertini, F. Casoli, P. Lupo, L. Nasi, M. Campanini, and A. Debernardi, Eur. Phys. J. B **86**, 211 (2013).

[22] A. Lamperti, E. Cianci, R. Ciprian, D. Sangalli, and A. Debernardi, Thin Solid Films **533**, 83 (2013).

[23] P. Satyarthi, S. Ghosh, P. Pandey, B.and Kumar, C. L. Chen, C. L.and Dong, W. F. Pong, D. Kanjilal, K. Asokan, and P. Srivastava, Journal of Applied Physics **113**, 183708 (2013), https://doi.org/10.1063/1.4804253.

[24] T. Higuchi, K. Kobayashi, S. Yamaguchi, A. Fukushima, S. Shin, and T. Tsukamoto, Japanese Journal of Applied Physics **42**, L941 (2003).

[25] D. H. Douma, R. Ciprian, A. Lamperti, P. Lupo, E. Cianci, D. Sangalli, F. Casoli, L. Nasi, F. Albertini, P. Torelli, and A. Debernardi, Phys. Rev. B **90**, 205201 (2014).

[26] L. Soriano, M. Abbate, J. Fuggle, J. Jiménez, M.A.and Sanz, and H. Mythen, C.and Padmore, Solid State Communications **87**, 699 (1993).

[27] D.-Y. Cho, H.-S. Jung, J. H. Kim, and C. S. Hwang, Applied Physics Letters **97**, 141905 (2010), https://doi.org/10.1063/1.3497077.

[28] A. Kikas, J. Aarik, V. Kisand, K. Kooser, T. Käämbre, H. Mändar, T. Uustare, R. Rammula, V. Sammelselg, and I. Martinson, Journal of Electron Spectroscopy and Related Phenomena **156-158**, 303 (2007), electronic Spectroscopy and Structure: ICESS-10.

[29] M. Abbate, F. M. F. de Groot, J. C. Fuggle, A. Fujimori, O. Strebel, F. Lopez, M. Domke, G. Kaindl, G. A. Sawatzky, M. Takano, Y. Takeda, H. Eisaki, and S. Uchida, Phys. Rev. B **46**, 4511 (1992).

[30] R. Kumar, A. P. Singh, P. Thakur, K. H. Chae, W. K. Choi, B. Angadi, S. D. Kaushik, and S. Patnaik, Journal of Physics D: Applied Physics **41**, 155002 (2008).

[31] P. Wu, G. Saraf, Y. Lu, D. Hill, R. Gateau, L. Wielunski, R. Bartynski, D. Arena, J. Dvorak, A. Moodenbaugh, *et al.*, Applied physics letters **89**, 012508 (2006).

[32] F. M. De Groot, P. Glatzel, U. Bergmann, P. A. van Aken, R. A. Barrea, S. Klemme, M. Hävecker, A. Knop-Gericke, W. M. Heijboer, and B. M. Weckhuysen, The Journal of Physical Chemistry B **109**, 20751 (2005).

[33] Although the total energies are computed after atomic relaxation, for convenience, in the presentation the distances in Fig. 5 are referred to the pristine flourite structure, i.e. before relaxation, since after relaxation atoms in the same shell can presents (sligtely) different distances from the central atoms, due the asymmetry introduced by the O vacancy and by the different magnetic coupling (AFM/FM) consitered.

[34] See, e.g. J. M. Coey, *Magnetism and Magnetic Materials* (Cambridge university press, Cambridge, 2009).

[35] For an illustration of super-exchange mechanism see e. g. N. Spaldin, *Magnetic Materials* (Cambridge University press, Cambridge). The interested reader can refer also to the original works: H. A. Kramers, Physica **1**, 182 (1934); P. W. Anderson, Phys. Rev. **79**, 350 (1950); J. B. Goodenough, *ibid.* **100**, 564 (1955).

[36] Similar result is expected also if the two (or few) FM coupled Fe have an AFM interaction with one Fe.

[37] A. I. Liechtenstein, M. I. Katsnelson, V. P. Antropov, and V. A. Gubanov, J. Magn. Magn. Mater. **67**, 65 (1987).

[38] L. M. Sandratskii and P. Bruno, Phys. Rev. B **66**, 134435 (2002).

[39] A. Ramasubramaniam and D. Naveh, Phys. Rev. B **87**, 195201 (2013).

[40] Y. D. Park, A. T. Hanbicki, S. C. Erwin, C. S. Hellberg, J. M. Sullivan, J. E. Mattson, T. F. Ambrose, A. Wilson, G. Spanos, and B. T. Jonker, Science **295**, 651 (2002).

[41] P. Mahadevan, A. Zunger, and D. D. Sarma, Phys. Rev. Lett. **93**, 177201 (2004).

[42] N. Ce-Wen, Materials Science and Engineering **B3**, L 1 (1989).